

pubs.acs.org/NanoLett Letter

# Multifunctional Metal—Oxide Nanocomposite Thin Film with Plasmonic Au Nanopillars Embedded in Magnetic La<sub>0.67</sub>Sr<sub>0.33</sub>MnO<sub>3</sub> Matrix

Jijie Huang,\* Han Wang, Zhimin Qi, Ping Lu, Di Zhang, Bruce Zhang, Zihao He, and Haiyan Wang\*



Cite This: Nano Lett. 2021, 21, 1032-1039



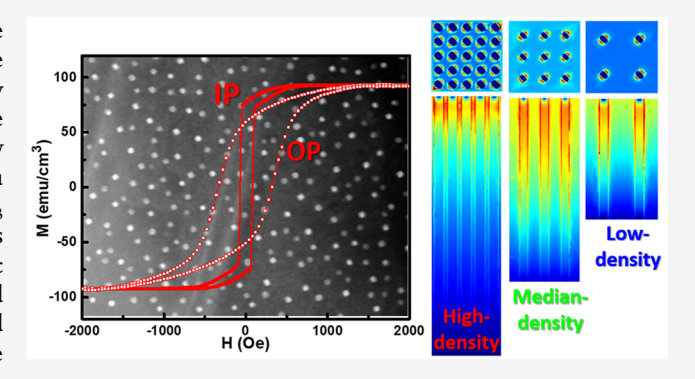
**ACCESS** I

III Metrics & More

Article Recommendations

S Supporting Information

ABSTRACT: Searching for multifunctional materials with tunable magnetic and optical properties has been a critical task toward the implementation of future integrated optical devices. Vertically aligned nanocomposite (VAN) thin films provide a unique platform for multifunctional material designs. Here, a new metal—oxide VAN has been designed with plasmonic Au nanopillars embedded in a ferromagnetic La<sub>0.67</sub>Sr<sub>0.33</sub>MnO<sub>3</sub> (LSMO) matrix. Such Au–LSMO nanocomposite presents intriguing plasmon resonance in the visible range and magnetic anisotropy property, which are functionalized by the Au and LSMO phase, respectively. Furthermore, the vertically aligned nanostructure of metal and dielectric oxide results in the hyperbolic property for near-field electromagnetic wave manipu-



lation. Such optical and magnetic response could be further tailored by tuning the composition of Au and LSMO phases.

KEYWORDS: Nanocomposite thin film, metal-oxide, plasmonic, magnetic anisotropic, hyperbolic

rtificial electromagnetic metamaterials with subwavelength scale metal nanostructures exhibit extraordinary optical performance, such as hyperbolic, negative refractive refraction, plasmonic etc., which allow their applications in subwavelength resolution imaging, photocatalysis, super lenses, cloaking, etc. 1-7 To date, various approaches have been developed to synthesize such metamaterials; one of the most popular methods is to electrodeposit metal nanorods into a porous anodic aluminum oxide (AAO) template, so-called template-assisted electrochemical deposition. 21/8-10 However, the size of the fabricated metal nanorods limits at 10 nm due to the size limitation of pore separation of the AAO template.1 Moreover, this method could only provide Al<sub>2</sub>O<sub>3</sub> as the oxide matrix, which hinders the further tuning of the optical properties by dielectric environment. In addition, the fragile nature of the AAO template hinders its scaling-up. Other developed methods include direct laser writing, electron-beam lithography, combined focused ion beam (FIB), etc., 12-14 which are all top-down lithography techniques.

Recently, a simple one-step pulsed laser deposition (PLD) technique has been applied to grow two-phase metal—oxide nanocomposite thin films, either by sequential deposition by multiple targets<sup>15–17</sup> or directly by a single mixed target.<sup>18–21</sup> Such method has been widely used for the growth of oxide—oxide vertically aligned nanocomposite (VAN) thin films previously.<sup>22,23</sup> For metal—oxide nanocomposite thin films, tremendous efforts have been invested for searching the proper

growth window to overcome the vastly different growth conditions for the metal and the oxide phases. Various metaloxide systems have been designed, from the functionality point of view, all of them could be divided into two categories, metal nanopillars with extraordinary optical performance <sup>19,21</sup> or anisotropic magnetic property. <sup>15–18,20</sup> For example, plasmonic Cu nanopillars embedded in ZnO have been fabricated, with hyperbolic and anisotropic optical properties.<sup>21</sup> On the other hand, ultrafine magnetic Co and Ni nanopillars have been introduced in different dielectric oxides, and anisotropic magnetic property has been obtained owing to the anisotropic nature of the nanopillars; such magnetic metal-oxide VAN thin films could be promising for high-density perpendicular recording media. 15-18,20 For all the previous designed metaloxide VANs, metal nanopillars are the effective part, while the oxide matrix typically works as the dielectric matrix for the metal nanopillars. Therefore, it is beneficial to design metaloxide systems with collective effects from both metal and oxide phases to achieve multifunctional metal-oxide VAN thin films.

Received: October 22, 2020 Revised: December 5, 2020 Published: January 6, 2021





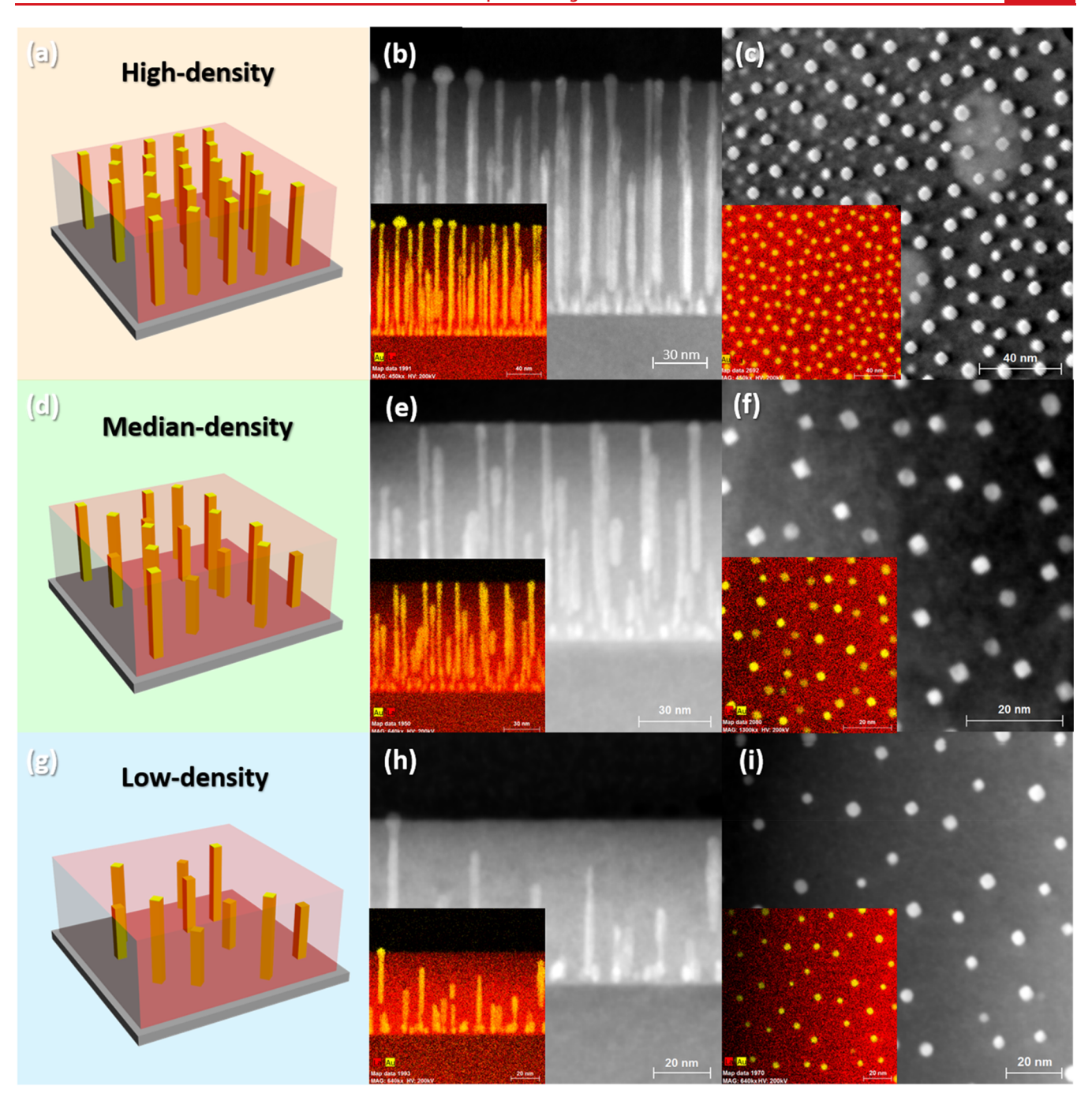


Figure 1. Schematic illustrations and microstructure of Au–LSMO nanocomposite thin films with different Au densities. (a) Schematic illustration, low-mag (b) cross-sectional and (c) plan-view STEM image with corresponding energy-dispersive X-ray spectroscopy (EDS) mapping of the high-density Au–LSMO thin film; (d) schematic illustration, low-mag (e) cross-sectional and (f) plan-view STEM image with corresponding EDS mapping of the median-density Au–LSMO thin film; (g) schematic illustration, low-mag (h) cross-sectional and (i) plan-view STEM image with corresponding EDS mapping of the low-density Au–LSMO thin film.

In this study, a new metal—oxide VAN has been designed with multifunctionalities from both phases, that is, plasmonic Au nanopillars embedded in ferromagnetic  $\text{La}_{0.67}\text{Sr}_{0.33}\text{MnO}_3$  (LSMO) matrix. LSMO is a perovskite-type manganese oxide material with fascinating magnetic (Curie temperature  $T_c$  of ~370 K) and transport properties owing to the double exchange mechanism. Furthermore, these properties can be tailored by oxygen stoichiometry, doping level, strain effect, and external pressure, and other owing to the interplay of lattice, spin, orbital, and charge in the material. Such lattice-spin-charge coupling allows LSMO to be widely used in

spintronic devices.<sup>33–35</sup> Therefore, LSMO is selected as the oxide matrix to achieve multifunctional Au–LSMO nanocomposite thin film, grown on SrTiO<sub>3</sub> (STO) substrate. The lattice parameter of STO (cubic, a=3.905 Å) is in between that of Au (cubic, a=4.072 Å) and LSMO (pseudocubic, a=3.873 Å), which allows the strain compensation effect to make the overall mismatch strain minimal and results in well-distributed Au nanopillars.<sup>36</sup> Overall, this Au–LSMO VAN is ideal for epitaxial nanocomposite thin film growth with multifunctionality, which opens up a new route toward multifunctional metal—oxide VAN designs.

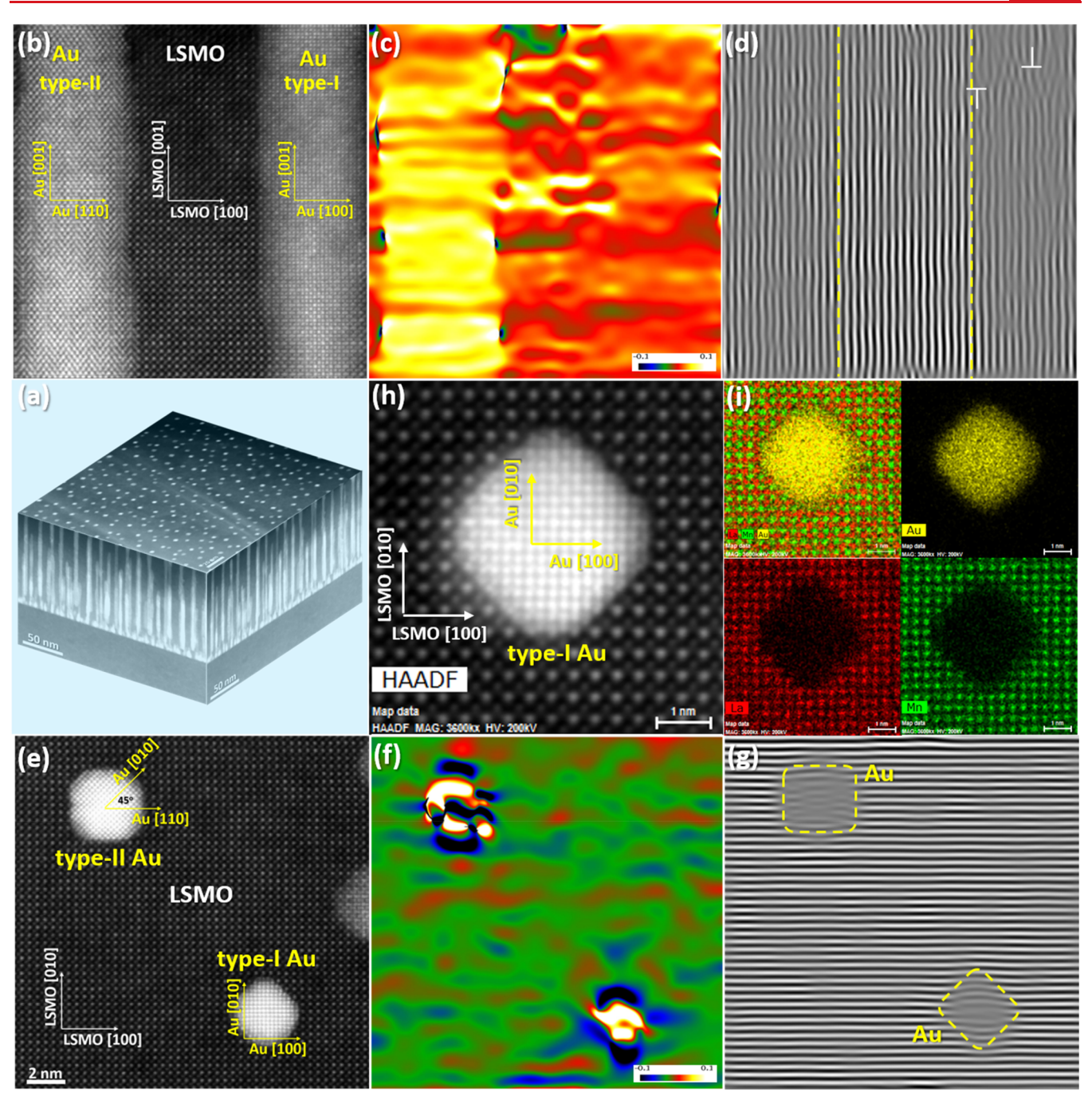
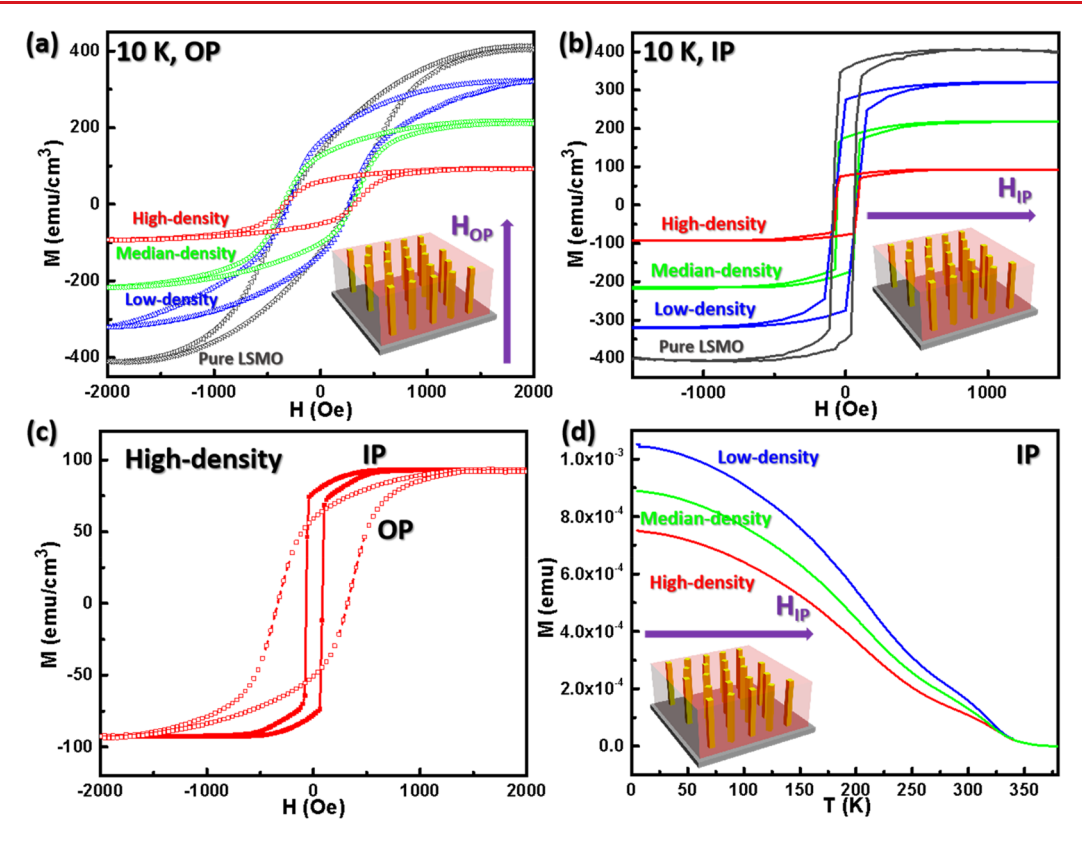


Figure 2. Detailed microstructure study of the high-density Au–LSMO nanocomposite thin film. (a) Overall 3-D image composed of low-mag cross-sectional and plan-view STEM images; (b) high-resolution cross-sectional STEM image with its corresponding (c) geometric phase analysis (GPA)  $\varepsilon_{yy}$  (out-of-plane strain) map and (d) masked inverse fast Fourier transform (FFT) image; (e) high-resolution plan-view STEM image with its corresponding (f) geometric phase analysis (GPA)  $\varepsilon_{yy}$  (in-plane strain) map and (g) masked inverse fast Fourier transform (FFT) image; (h) high-resolution STEM image of one type-I Au nanopillar and (i) its corresponding EDS elemental mapping.

Results and Discussion. Au–LSMO VANs with different Au contents refer to high-density, median-density, and low-density Au–LSMO. A pure LSMO film has also been grown for comparison. Figure S1suggests the excellent epitaxial quality of all the films, and it is worth noting that two types of Au domains with 45° rotation have been obtained (see details in Supporting Information). Then scanning transmission electron microscopy (STEM) has been conducted in both cross-sectional and plan-view directions to construct the 3-D view of the Au–LSMO VANs with different Au nanopillar densities, as shown in Figure 1. For the high-density sample

(cross-section in Figure 1b and plan-view in Figure 1c, with EDS mapping as inserted), most of the Au nanopillars grow straight throughout the entire thickness of the film. Additional STEM images in Figure S2 cover a large area of the film, which demonstrate the well-distributed Au nanopillars in large scale. While Au content reduces to median-density, some of the Au nanopillars cease to grow in halfway, as shown in Figure 1e and f for cross-sectional and plan-view (with EDS mapping as inserted), respectively. Furthermore, in the low-density Au–LSMO, most of the Au nanopillars failed to grow throughout the entire thickness due to insufficient Au source during



**Figure 3.** Magnetic properties of Au–LSMO nanocomposite thin films with different Au densities. Comparison of magnetization—field hysteresis loops of the Au–LSMO nanocomposite thin films and the pure LSMO film, with applied magnetic field in (a) OP (perpendicular to film surface) and (b) IP (parallel to film surface) measured at 10 K; (c) comparison of the OP M-H and IP M-H curves of the high-density Au–LSMO to demonstrate the anisotropic magnetic property; (d) magnetization—temperature (5–380 K) curves of the Au–LSMO nanocomposite thin films with applied magnetic field in IP direction.

deposition as shown in Figure 1h and i for cross-sectional and plan-view (with EDS mapping as inserted), respectively. Finally, the 3-D construction of high-density, median-density, and low-density samples can be built in the schematic illustrations in Figure 1a, d, and g, respectively.

To further explore the microstructure and strain state in high-density Au-LSMO, a detailed high-resolution TEM analysis has been conducted. Figure 2a is a 3-D view of the sample constructed by low-mag cross-sectional and plan-view STEM images to show the overall morphology. Figure 2b presents a high-resolution STEM image containing two different Au nanopillars, type-I with Au [001]/LSMO [001], Au [100]/LSMO [100] and type-II with Au [001]/LSMO [001], Au [110]/LSMO [100], which is consistent with the XRD results. The corresponding geometric phase analysis (GPA) has been carried out to reveal the strain state in each phase, as shown in Figure 2c. Compressive strain has been generated in the Au-LSMO interface area, while apparent tensile strain appears inside the Au nanopillars. The corresponding inverse fast Fourier transform (FFT) image has also been shown in Figure 2d to investigate the film quality. Very limited dislocations have been identified, and distorted lattices can be observed to compensate the lattice mismatch. High-resolution plan-view STEM image has been shown in Figure 2e to further explore its detailed microstructure, again both type I and type II Au nanopillars can be observed. Its corresponding GPA and inverse FFT images are presented in Figure 2f and g, respectively, to probe the strain state in horizontal point of view. Both indicate the high strain state in

the Au–LSMO interface and inside Au nanopillars to ensure the excellent epitaxial quality of the nanocomposite film. The high quality of the film has been further confirmed by atomic-scale STEM and its corresponding EDS mapping, as shown in Figure 2h and i, respectively, which includes one type-I Au nanoparticle. The images containing type-II Au nanoparticles are exhibited in Figure S3. As seen, clear and abrupt Au–LSMO interfaces are presented for both type-I Au–LSMO and type-II Au–LSMO interfaces, which suggests no or very limited interdiffusion occurs between the metal and oxide phase. Overall, the high-density Au–LSMO nanocomposite thin film shows well-distributed Au nanopillars with excellent epitaxial quality for both phases.

To reveal the multifunctionality of the designed Au-LSMO nanocomposite thin films, magnetic measurements were first conducted. Figure 3a and b compare the *M*–*H* curves (10 K) of the three Au-LSMO films and a pure LSMO reference sample with applied magnetic field perpendicular (OP: out-ofplane) and parallel (IP: in-plane) to the film surface, respectively. All of the samples exhibit significant ferromagnetic response with the low-density Au-LSMO obtaining the highest saturation magnetization (M<sub>s</sub>) in both OP and IP directions among the nanocomposite films, as this sample contains the most amount of LSMO, which contributes to the ferromagnetic response (note that we used the volume of the entire film to calculate M). However, the coercivity  $(H_c)$  of all the samples are the same since this is mostly a natural property of LSMO. The room-temperature M-H comparison is also presented in Figure S4, which exhibits the similar shape of the

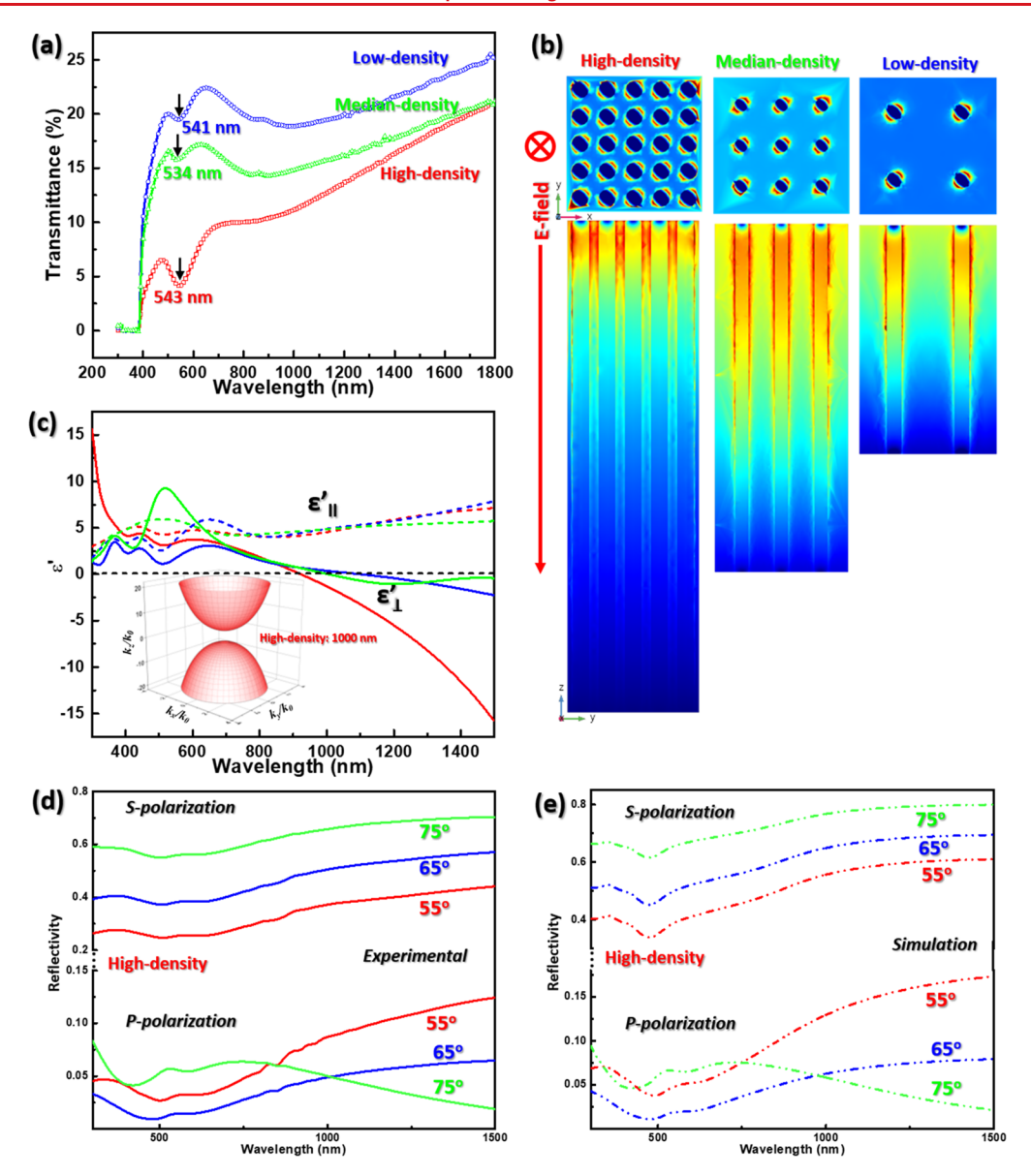


Figure 4. Optical measurements of Au–LSMO nanocomposite thin films with different Au densities. (a) Transmittance spectral of the films (300–1800 nm); (b) COMSOL simulated optical field enhancement maps corresponding to incident illumination at 550 nm in both in-plane (upper panel) and out-of-plane (lower panel) view directions; (c) real part of complex dielectric function (e') of the Au–LSMO thin films, biaxial geometry is applied to extract e' (OP  $e_{\perp}'$ , dashed lines; IP  $e_{\parallel}'$ , solid lines) of the Au–LSMO nanocomposite thin films, inset is the extracted isofrequency surfaces of the high-density Au–LSMO film at 1000 nm;  $k_0 = w/c$  is the wavenumber in vacuum;  $k_x$ ,  $k_y$ , and  $k_z$  are the [100], [010], and [001] components of the wavevector, respectively; (d) experimental and (e) simulated reflectivity spectra of the high-density Au–LSMO for different angles (55°, 65°, and 75°) of incidence for both s-polarized and p-polarized incident lights.

curves with the reduced absolute M values. Figure 3c shows the very different OP and IP M-H loops (10 K) of the high-density Au–LSMO, which suggests the magnetic anisotropy in the films. Magnetic anisotropy is well-known in LSMO, especially in the form of thin film, which can be utilized for high-density energy-storage magnets. Such magnetic anisotropy could be tailored by the strain state in the film as well as film thickness. <sup>37,38</sup> Here, the anisotropic nature of the LSMO matrix and the vertical strain induced by the Au/LSMO lattice mismatch could also contribute to the overall magnetic anisotropy of the film. Furthermore, magnetization—temperature (M-T) curves have been measured and plotted in Figure 3d and Figure S5 for IP and OP, respectively. The  $T_c$  of the films can be determined at ~350 K, which is a little lower than the value of ~370 K. This  $T_c$  reduction could be ascribed to

the suppressed double-exchange coupling by the disordered phase or grain boundaries.  $^{39}$ 

Besides the intriguing magnetic properties, optical property could be another interesting feature of this Au–LSMO nanocomposite thin films. First, transmittance spectral measurement (wavelength range: 300–1800 nm) of the nanocomposite films has been carried out and compared in Figure 4a. Apparently, surface plasmon resonance (SPR) has been observed for all the three samples, and the transmittance dip becomes deeper with increasing Au density, which indicates that such SPR is resulted from the Au nanopillars. In addition, the SPR wavelength is located at 541, 534, and 543 nm for the low-density, median-density, and high-density samples, respectively, the minor difference might be caused by the shape and size difference of the Au nanopillars as well as

the hybridization from coupling among the neighboring nanopillars. Such SPR feature has been further confirmed by the COMSOL simulated optical field enhancement maps (at 550 nm, which is close to the SPR position) shown in Figure 4b for all the samples. The pronounced plasmonic feature could be attributed to the Au nanopillars themselves as well as the Au–LSMO interfaces. However, no obvious resonance is observed with 1000 nm incident light (Figure S6), as it is far away from the SPR position.

To probe the anisotropic optical performance of such Au-LSMO VAN films, angular-dependent ellipsometry measurements have been conducted. The ellipsometric phi  $(\phi)$  values shown in Figure S7 are used to derive the optical complex dielectric functions (real part  $\varepsilon'$  and imaginary part  $\varepsilon''$ ) of all the Au-LSMO VAN films. Here, for the Au-LSMO VAN films, we built a uniaxial model for the fitting due to their anisotropic nature; the comparison of  $\varepsilon'$  and  $\varepsilon''$  is presented in Figure 4b and Figure S8, respectively. For the real part  $\varepsilon'$ ,  $\varepsilon_{\parallel}$ (parallel to the film surface) is positive throughout the entire fitted wavelength up to 1500 nm for all the three samples, while  $\varepsilon_{\perp}{}'$  (perpendicular to the film surface) starts to turn into negative at 923, 1010, and 1100 nm for the high-density, median-density, and low-density Au-LSMO, respectively. This implies that Au-LSMO is an ideal hyperbolic metamaterial (HMM) with a transverse-positive dispersion, which could be integrated in optical devices such as a hyperlens.<sup>40</sup> To further comprehend the optical anisotropy of the Au-LSMO VANs, iso-frequency k-space surface (at 1000 nm) has been plotted for the high-density film to probe its optical iso-frequency surface, as shown in the inserted image in Figure 4b. Au-LSMO film can be identified as uniaxially anisotropic material  $(\varepsilon[100] = \varepsilon[010] \neq \varepsilon[001])$ , so its electromagnetic wave (kwavevector) could be manifested by the dispersion relation:

$$\frac{k_x^2 + k_y^2}{\varepsilon_{\perp}} + \frac{k_z^2}{\varepsilon_{\parallel}} = \frac{\omega^2}{c^2} = k_0^2$$

Here,  $k_x$ ,  $k_y$ , and  $k_z$  are the components of the wave vector in the direction of parallel and perpendicular to the film surface; w is the frequency; and c is the speed of light. Iso-frequency kspace surface (at 1200 nm) for the median-density and lowdensity films is also shown in Figure S9. All three samples exhibit a hyperbola shape with two sheets, which is a sign of type II hyperbolic metamaterial. Lastly, we used angulardependent and polarization-resolved reflectivity measurement (incident angles of  $55^\circ,\,65^\circ,$  and  $75^\circ$  for both s-polarized and p-polarized light) to obtain the reflectivity spectral of all the films, as plotted in Figure 4c for the high-density film. Moreover, the reflectivity has been simulated by different models in VASE software, and the simulated reflectivity spectral well reproduces the experimental data, as shown in Figure 4d. The experimental and simulated reflectivity for the median-density and low-density samples are presented in Figure S10, which again match each other well for both the intensity and trend throughout the measured wavelength.

The implication of this Au–LSMO nanocomposite thin film is to meet the great demand of multifunctional materials for different device designs. The demonstration of Au–LSMO could be extended to other metal–oxide systems for multifunctionalities. For example, the combination of ferromagnetic Co with ferroelectric BaTiO<sub>3</sub> (BTO) forms a multiferroic system, which could rarely be achieved in single phase material.<sup>41</sup> In addition, the size of the Au nanopillars

could be tailored by careful deposition parameter control, for example, laser frequency<sup>18</sup> or growth temperature. <sup>42</sup> Furthermore, a new physical phenomenon might be discovered in the metal—oxide interface because of the interplay of photon, electron, spin, and lattice in each phase. For practical applications, future effort could focus on the magnetron sputtering growth of such a nanocomposite thin film, which has been realized in the growth of both metal—oxide <sup>43,44</sup> and oxide—oxide systems. <sup>45</sup> Overall, the design of metal—oxide hybrid systems present significant potentials from both device integration and fundamental physics point of view.

**Conclusions.** Self-assembled Au–LSMO nanocomposite thin films with different Au nanopillar densities have been obtained by a one-step PLD method. Both Au and LSMO show excellent epitaxial quality, with the nanostructure of Au nanopillars vertically aligned in the LSMO matrix. Plasmon resonance occurs in the wavelength range from 534–543 nm for Au–LSMO with different Au nanopillar densities. Anisotropic magnetic property is achieved by the LSMO phase, with  $T_{\rm c}$  of ~350 K. In addition, the unique VAN structure results in optical anisotropy response, which is,  $\varepsilon'$  in vertical and horizontal directions starting to show opposite sign in the near-infrared wavelength range. The anisotropic optical performance has been further confirmed by angle-dependent and polarization-resolved reflectivity measurement, which makes it ideal as a hyperbolic metamaterial.

**Experimental Section.** Thin Film Deposition. The Au–LSMO thin films have been deposited on single crystal STO (001) wafers using a pulsed laser deposition technique with a KrF excimer laser (Lambda Physik CompexPro 205,  $\lambda = 248$  nm, 5 Hz). A conventional LSMO target was used as the LSMO source along with a thin Au foil as the Au source. The different Au composition can be achieved by varying the area of the Au foils on the LSMO target. Before deposition, the base pressure has been pumped down to lower than  $1 \times 10^{-6}$  Torr. During deposition, the substrate temperature has been kept at 700 °C with 50 mTorr O<sub>2</sub> in-flowing. The deposition was done by a laser frequency of 5 Hz with the total of 5000 pulses. After deposition, the samples have been naturally cooled down to room temperature with 50 mTorr O<sub>2</sub> in the chamber.

Microstructure Characterization. XRD (Panalytical X'Pert X-ray diffractometer) has been used for the crystallinity characterization. FEI Titan G2 80–200 microscope with a Cs probe corrector and TEAM 0.5, a modified FEI Titan microscope with a special high-brightness Schottky field emission electron source, and an improved hexapole-type illumination aberration corrector have been employed to take the STEM images in HAADF mode.

Magnetic Measurements. Temperature dependence magnetization (2–380 K) and magnetic hysteresis curves (–2000–2000 Oe) have been measured by a SQUID magnetometer (MPMS: Quantum Design), with the applied field direction either perpendicular or parallel to the film surface.

Optical Measurements. Transmittance spectra have been taken by UV–visible spectroscopy (Lambda 1050). Variable angle ellipsometry experiments have been conducted using a RC2 spectroscopic ellipsometer (J.A. Woollam Company). Two parameters of Psi ( $\varphi$ ) and Delta ( $\Delta$ ) were collected by the ellipsometry measurements, which are correlated with the ratio of the reflection coefficients for the light of p-polarization  $r_{\rm p}$  and s-polarization  $r_{\rm s}$ :  $r_{\rm p}/r_{\rm s}=\tan(\varphi)\exp(i\Delta)$ . Then the effective refractive index and optical dielectric constants can be

obtained by fitting the ellipsometry data with certain models. Angle-dependent and polarization-resolved reflectivity measurement (incident angles of 55°, 65°, and 75°) has been applied to measure the reflectivity of the films.

## ASSOCIATED CONTENT

# Supporting Information

The Supporting Information is available free of charge at https://pubs.acs.org/doi/10.1021/acs.nanolett.0c04213.

XRD comparison of Au–LSMO films; additional STEM images of high-density Au–LSMO; M-H hysteresis loop comparison at room-temperature; M–T curves of films in OP direction; COMSOL simulated optical field maps corresponding to incident illumination at 1000 nm; experimental and fitted ellipsometric parameter ( $\varphi$ ) vs wavelength; imaginary part of complex dielectric function (e''); extracted iso-frequency surfaces of median- and low-density Au–LSMO film at wavelength of 1200 nm; experimental and simulated reflectivity spectra of median- and low-density Au–LSMO (PDF)

#### AUTHOR INFORMATION

# **Corresponding Authors**

Jijie Huang — School of Materials, Sun Yat-sen University, Guangzhou, Guangdong 510275, China; Email: huangjj83@mail.sysu.edu.cn

Haiyan Wang — School of Materials Engineering and School of Electrical and Computer Engineering, Purdue University, West Lafayette, Indiana 47906, United States; oorcid.org/0000-0002-7397-1209; Email: hwang00@purdue.edu

# Authors

Han Wang — School of Materials Engineering, Purdue University, West Lafayette, Indiana 47906, United States; orcid.org/0000-0002-6137-4802

Zhimin Qi – School of Materials Engineering, Purdue
 University, West Lafayette, Indiana 47906, United States

 Ping Lu – Sandia National Laboratories, Albuquerque, New
 Mexico 87185, United States

Di Zhang – School of Materials Engineering, Purdue University, West Lafayette, Indiana 47906, United States

Bruce Zhang — School of Electrical and Computer Engineering, Purdue University, West Lafayette, Indiana 47906, United States

Zihao He — School of Electrical and Computer Engineering, Purdue University, West Lafayette, Indiana 47906, United States

Complete contact information is available at: https://pubs.acs.org/10.1021/acs.nanolett.0c04213

#### **Notes**

The authors declare no competing financial interest.

## ACKNOWLEDGMENTS

This work was supported by the U.S. Department of Energy, Office of Science, Basic Energy Sciences under Award No. DE-SC0020077. The high resolution STEM effort was supported by the U.S. National Science Foundation (DMR-1565822 and DMR-1809520). J.H. acknowledges the support from Guangdong Basic and Applied Basic Research Foundation (2019A1515111029). Sandia National Laboratories is a multimission laboratory managed and operated by National

Technology and Engineering Solutions of Sandia, LLC., a wholly owned subsidiary of Honeywell International, Inc., for the U.S. Department of Energy's National Nuclear Security Administration under Contract No. DE-NA0003525. This paper describes objective technical results and analysis. Any subjective views or opinions that might be expressed in the paper do not necessarily represent the views of the U.S. Department of Energy or the United States Government.

#### REFERENCES

- (1) Poddubny, A.; Iorsh, I.; Belov, P.; Kivshar, Y. Hyperbolic Metamaterials. *Nat. Photonics* **2013**, *7*, 958–962.
- (2) Yao, J.; Liu, Z.; Liu, Y.; Wang, Y.; Sun, C.; Bartal, G.; Stacy, A.; Zhang, X. Optical Negative Refraction in Bulk Metamaterials of Nanowires. *Science* **2008**, *321* (5891), 930.
- (3) Linic, S.; Christopher, P.; Ingram, D. Plasmonic-Metal Nanostructures for Efficient Conversion of Solar to Chemical Energy. *Nat. Mater.* **2011**, *10* (12), 911–921.
- (4) Barnes, W. L.; Dereux, A.; Ebbesen, T. W. Surface Plasmon Subwavelength Optics. *Nature* **2003**, 424 (6950), 824–830.
- (5) Christopher, P.; Xin, H.; Linic, S. Visible-Light-Enhanced Catalytic Oxidation Reactions on Plasmonic Silver Nanostructures. *Nat. Chem.* **2011**, *3*, 467–472.
- (6) Zhang, X.; Liu, Z. W. Superlenses to Overcome the Diffraction Limit. *Nat. Mater.* **2008**, *7* (6), 435–441.
- (7) Valentine, J.; Li, J.; Zentgraf, T.; Bartal, G.; Zhang, X. An Optical Cloak Made of Dielectrics. *Nat. Mater.* **2009**, 8 (7), 568–571.
- (8) Evans, P.; Kullock, R.; Hendren, W.; Atkinson, R.; Pollard, R.; Eng, L. Optical Transmission Properties and Electric Field Distribution of Interacting 2D Silver Nanorod Arrays. *Adv. Funct. Mater.* **2008**, *18*, 1075–1079.
- (9) Masuda, H.; Fukuda, K. Ordered Metal Nanohole Arrays Made by a Two-Step Replication of Honeycomb Structures of Anodic Alumina. *Science* **1995**, *268*, 1466–1468.
- (10) Kabashin, A. V.; Evans, P.; Pastkovsky, S.; Hendren, W.; Wurtz, G. A.; Atkinson, R.; Pollard, R.; Podolskiy, V. A.; Zayats, A. V. Plasmonic Nanorod Metamaterials for Biosensing. *Nat. Mater.* **2009**, 8 (11), 867–871.
- (11) Lee, S.; Guan, Z.; Xu, H.; Moskovits, M. Surface-Enhanced Raman Spectroscopy and Nanogeometry: The Plasmonic Origin of SERS. *J. Phys. Chem. C* **2007**, *111*, 17985–17988.
- (12) Gansel, J. K.; Thiel, M.; Rill, M. S.; Decker, M.; Bade, K.; Saile, V.; von Freymann, G.; Linden, S.; Wegener, M. Gold Helix Photonic Metamaterial as Broadband Circular Polarizer. *Science* **2009**, 325 (5947), 1513–1515.
- (13) Liu, N.; Guo, H. C.; Fu, L. W.; Kaiser, S.; Schweizer, H.; Giessen, H. Three-Dimensional Photonic Metamaterials at Optical Frequencies. *Nat. Mater.* **2008**, *7* (1), 31–37.
- (14) Melosh, N.; Boukai, A.; Diana, F.; Gerardot, B.; Badolato, A.; Petroff, P.; Heath, J. Ultrahigh-Density Nanowire Lattices and Circuits. *Science* **2003**, *300*, 112–115.
- (15) Bonilla, F.; Novikova, A.; Vidal, F.; Zheng, Y.; Fonda, E.; Demaille, D.; Schuler, V.; Coati, A.; Vlad, A.; Garreau, Y.; Sauvage Simkin, M.; Dumont, Y.; Hidki, S.; Etgens, V. Combinatorial Growth and Anisotropy Control of Self-Assembled Epitaxial Ultrathin Alloy Nanowires. *ACS Nano* **2013**, *7* (5), 4022–4029.
- (16) Hennes, M.; Schuler, V.; Weng, X.; Buchwald, J.; Demaille, D.; Zheng, Y.; Vidal, F. Growth of Vertically Aligned Nanowires in Metal-Oxide Nanocomposites: Kinetic Monte-Carlo Modeling Versus Experiments. *Nanoscale* **2018**, *10*, 7666–7675.
- (17) Shin, J.; Goyal, A.; Cantoni, C.; Sinclair, J.; Thompson, J. Self-Assembled Ferromagnetic Cobalt/Yttria-Stabilized Zirconia Nanocomposites for Ultrahigh Density Storage Applications. *Nanotechnology* **2012**, *23*, 155602.
- (18) Huang, J.; Li, L.; Lu, P.; Qi, Z.; Sun, X.; Zhang, X.; Wang, H. Self-Assembled Co-BaZrO<sub>3</sub> Nanocomposite Thin Films with Ultra-Fine Vertically Aligned Co Nanopillars. *Nanoscale* **2017**, *9*, 7970–7976.

- (19) Li, L.; Sun, L.; Gomez-Diaz, J.; Hogan, N.; Lu, P.; Khatkhatay, F.; Zhang, W.; Jian, J.; Huang, J.; Su, Q.; Fan, M.; Jacob, C.; Li, J.; Zhang, X.; Jia, Q.; Sheldon, M.; Alú, A.; Li, X.; Wang, H. Self-Assembled Epitaxial Au—Oxide Vertically Aligned Nanocomposites for Nanoscale Metamaterials. *Nano Lett.* **2016**, *16*, 3936—3943.
- (20) Huang, J.; Qi, Z.; Li, L.; Wang, H.; Xue, S.; Zhang, B.; Zhang, X.; Wang, H. Self-Assembled Vertically Aligned Ni Nanopillars in CeO<sub>2</sub> with Anisotropic Magnetic and Transport Properties for Energy Applications. *Nanoscale* **2018**, *10*, 17182–17188.
- (21) Huang, J.; Wang, X.; Phuah, X.; Lu, P.; Qi, Z.; Wang, H. Plasmonic Cu Nanostructures in ZnO as Hyperbolic Metamaterial Thin Films. *Materials Today Nano* **2019**, *8*, 100052.
- (22) MacManus-Driscoll, J.; Suwardi, A.; Wang, H. Composite Epitaxial Thin Films: A New Platform for Tuning, Probing, and Exploiting Mesoscale Oxides. MRS Bull. 2015, 40, 933–942.
- (23) Huang, J.; MacManus-Driscoll, J.; Wang, H. New Epitaxy Paradigm in Epitaxial Self-Assembled Oxide Vertically Aligned Nanocomposite Thin Films. *J. Mater. Res.* **2017**, 32 (21), 4054–4066.
- (24) Goodenough. Theory of the Role of Covalence in the Perovskite-Type Manganites [La, M(II)]MnO<sub>3</sub>. Phys. Rev. 1955, 100, 564.
- (25) Dey, P.; Nath, T.; Taraphder, A. Effect of Substrate-Induced Strain on Transport and Magnetic Properties of Epitaxial La<sub>0.66</sub>Sr<sub>0.33</sub>MnO<sub>3</sub> Thin Films. *Appl. Phys. Lett.* **2007**, *91*, No. 012511.
  (26) Park, J. H.; Vescovo, E.; Kim, H.-J.; Kwon, C.; Ramesh, R.;
- Venkatesan, T. Direct Evidence for a Half-Metallic Ferromagnet. *Nature* **1998**, 392, 794–796.
- (27) Huang, J.; Wang, H.; Sun, X.; Zhang, X.; Wang, H. Multifunctional La<sub>0,67</sub>Sr<sub>0,33</sub>MnO<sub>3</sub>(LSMO) Thin Films Integrated on Mica Substrates toward Flexible Spintronics and Electronics. *ACS Appl. Mater. Interfaces* **2018**, *10*, 42698–42705.
- (28) Panchal, G.; Phase, D.; Reddy, V.; Choudhary, R. Strain-Induced Elastically Controlled Magnetic Anisotropy Switching in Epitaxial La<sub>0.7</sub>Sr<sub>0.3</sub>MnO<sub>3</sub> Thin Films on BaTiO<sub>3</sub>(001). *Phys. Rev. B: Condens. Matter Mater. Phys.* **2018**, 98, No. 045417.
- (29) Picozzi, S.; Ma, C.; Yang, Z.; Bertacco, R.; Cantoni, M.; Cattoni, A.; Petti, D.; Brivio, S.; Ciccacci, F. Oxygen Vacancies and Induced Changes in the Electronic and Magnetic Structures of La<sub>0.66</sub>Sr<sub>0.33</sub>MnO<sub>3</sub>: A Combined ab initio and Photoemission study. *Phys. Rev. B: Condens. Matter Mater. Phys.* **2007**, *75*, No. 094418.
- (30) Urushibara, A.; Moritomo, Y.; Arima, T.; Asamitsu, A.; Kido, G.; Tokura, Y. Insulator-Metal Transition and Giant Magnetoresistance in La<sub>1-x</sub>Sr<sub>x</sub>MnO<sub>3</sub>. *Phys. Rev. B: Condens. Matter Mater. Phys.* **1995**, *51*, 14103.
- (31) Vailionis, A.; Boschker, H.; Siemons, W.; Houwman, E. P.; Blank, D. H. A.; Rijnders, G.; Koster, G. Misfit Strain Accommodation in Epitaxial ABO<sub>3</sub> Perovskites: Lattice Rotations and Lattice Modulations. *Phys. Rev. B: Condens. Matter Mater. Phys.* **2011**, 83, No. 064101.
- (32) Hwang, H.; Palstra, T.; Cheong, S.; Batlogg, B. Pressure Effects on the Magnetoresistance in Doped Manganese Perovskites. *Phys. Rev. B: Condens. Matter Mater. Phys.* **1995**, *52*, 15046.
- (33) Sun, D.; Yin, L.; Sun, C.; Guo, H.; Gai, Z.; Zhang, X. G.; Ward, T.; Cheng, Z.; Shen, J. Giant Magnetoresistance in Organic Spin Valves. *Phys. Rev. Lett.* **2010**, *104*, 236602.
- (34) Pincelli, T.; Lollobrigida, V.; Borgatti, F.; Regoutz, A.; Gobaut, B.; Schlueter, C.; Lee, T.-L.; Payne, D. J.; Oura, M.; Tamasaku, K.; Petrov, A. Y.; Graziosi, P.; Granozio, F. M.; Cavallini, M.; Vinai, G.; Ciprian, R.; Back, C. H.; Rossi, G.; Taguchi, M.; Daimon, H.; et al. Quantifying the Critical Thickness of Electron Hybridization in Spintronics Materials. *Nat. Commun.* **2017**, *8*, 16051.
- (35) Wahler, M.; Homonnay, N.; Richter, T.; Müller, A.; Eisenschmidt, C.; Fuhrmann, B.; Schmidt, G. Inverse Spin Hall Effect in a Complex Ferromagnetic Oxide Heterostructure. *Sci. Rep.* **2016**, *6*, 28727.
- (36) Huang, J.; Wang, X.; Hogan, N.; Wu, S.; Lu, P.; Fan, Z.; Dai, Y.; Zeng, B.; Starko-Bowes, R.; Jian, J.; Wang, H.; Li, L.; Prasankumar, R.; Yarotski, D.; Sheldon, M.; Chen, H.; Jacob, Z.; Zhang, X.; Wang, H. Nanoscale Artificial Plasmonic Lattice in Self-Assembled Vertically

- Aligned Nitride-Metal Hybrid Metamaterials. Adv. Sci. 2018, 6, 1800416.
- (37) Tsui, F.; Smoak, M.; Nath, T.; Eom, C. Strain-Dependent Magnetic Phase Diagram of Epitaxial La<sub>0.67</sub>Sr<sub>0.33</sub>MnO<sub>3</sub> Thin Films. *Appl. Phys. Lett.* **2000**, *76*, 2421.
- (38) Steenbeck, K.; Habisreuther, T.; et al. Magnetic Anisotropy of Ferromagnetic La<sub>0.7</sub>Sr<sub>0.3</sub>MnO<sub>3</sub> Epitaxial Thin Films: Dependence on Temperature and Film Thickness. *Appl. Phys. Lett.* **2002**, *80*, 3361.
- (39) Rivadulla, F.; Otero-Leal, M.; Espinosa, A.; de Andres, A.; Ramos, C.; Rivas, J.; Goodenough, J. B. Suppression of Ferromagnetic Double Exchange by Vibronic Phase Segregation. *Phys. Rev. Lett.* **2006**, *96*, No. 016402.
- (40) Jacob, Z.; Alekseyev, L.; Narimanov, E. Optical Hyperlens: Far-Field Imaging beyond the Diffraction Limit. *Opt. Express* **2006**, *14*, 8247–8256.
- (41) Wang, J.; Neaton, J.; Zheng, H.; Nagarajan, V.; Ogale, S.; Liu, B.; Viehland, D.; Vaithyanathan, V.; Schlom, D.; Waghmare, U.; Spaldin, N.; Rabe, K.; Wuttig, M.; Ramesh, R. Epitaxial BiFeO<sub>3</sub> Multiferroic Thin Film Heterostructures. *Science* **2003**, 299 (5613), 1719–1722.
- (42) Su, Q.; Zhang, W.; Lu, P.; Fang, S.; Khatkhatay, F.; Jian, J.; Li, L.; Chen, F.; Zhang, X.; MacManus-Driscoll, J.; Chen, A.; Jia, Q.; Wang, H. Self-Assembled Magnetic Metallic Nanopillars in Ceramic Matrix with Anisotropic Magnetic and Electrical Transport Properties. ACS Appl. Mater. Interfaces 2016, 8, 20283–20291.
- (43) Gao, J.; Wu, X.; Li, Q.; Du, S.; Huang, F.; Liang, L.; Zhang, H.; Zhuge, F.; Cao, H.; Song, Y. Template-Free Growth of Well-Ordered Silver Nano Forest/Ceramic Metamaterial Films with Tunable Optical Responses. *Adv. Mater.* 2017, 29, 1605324.
- (44) Hu, H.; Gao, W.; Zang, R.; Gao, J.; Tang, S.; Li, X.; Liang, L.; Zhang, H.; Cao, H. Direct Growth of Vertically Orientated Nanocavity Arrays for Plasmonic Color Generation. *Adv. Funct. Mater.* **2020**, *30*, 2002287.
- (45) Kim, T.; Ojha, S.; Tian, G.; Lee, S.; Jung, H.; Choi, J.; Kornblum, L.; Walker, F.; Ahn, C.; Ross, C.; Kim, D. Self-Assembled Multiferroic Epitaxial BiFeO<sub>3</sub>-CoFe<sub>2</sub>O<sub>4</sub> Nanocomposite Thin Films Grown by RF Magnetron Sputtering. *J. Mater. Chem. C* **2018**, *6*, 5552–5561.